Deformation and metasomatism recorded by single-grain apatite petrochronology

Margaret L. Odlum[1], Drew A. Levy[2], Daniel F. Stockli[3], Lisa D. Stockli[3] and Joel W. DesOrmeau[2]

[1]Department of Geoscience, University of Nevada, Las Vegas, Nevada 89154, USA
[2]Department of Geological Sciences & Engineering, University of Nevada, Reno, Nevada 89557, USA
[3]Department of Geological Sciences, University of Texas at Austin, Austin, Texas 78712, USA

ABSTRACT

The timing and processes of ductile deformation and metasomatism can be documented using apatite petrochronology. We integrated microstructural, U-Pb, and geochemical analyses of apatite grains from an exhumed mylonitic shear zone in the St. Barthélémy Massif, Pyrenees, France, to understand how deformation and metasomatism are recorded by U-Pb dates and geochemical patterns. Electron backscatter diffraction (EBSD) analyses documents crystal plastic deformation characterized by low-angle boundaries (<5°) associated with dislocation creep and evidence of multiple slip systems. Laser ablation–inductively coupled plasma–mass spectrometry (LA-ICP-MS) U-Pb maps indicate that dates in deformed grains reflect, and are governed by, low-angle dislocation boundaries. Apatite rare earth element (REE) and U-Pb behavior is decoupled in high-grade gneiss samples, suggesting REEs record higher-temperature processes than U-Pb isotopic systems. Apatite from (ultra)mylonitic portions of the shear zone showed evidence of metasomatism, and the youngest dates constrain the age of metasomatism. Collectively, these results demonstrate that crystal plastic microstructures and fluid interactions can markedly change apatite isotopic signatures, making single-grain apatite petrochronology a powerful tool for dating and characterizing the latest major deformation and/or fluid events, which are often not captured by higher-temperature chronometers.

INTRODUCTION

Chronologic constraints paired with microstructural and geochemical information (i.e., petrochronology) are critical for understanding the pressure-temperature-time (*P-T-t*) evolution of ductile deformation and metasomatism. Resetting of U-Pb dates by crystal plastic deformation can directly date deformation events if dates can be linked to deformation-related textures (e.g., Reddy and Potts, 1999; Erickson et al., 2015) in zircon (e.g., Reddy et al., 2007; Piazolo et al., 2012), monazite (e.g., Erickson et al., 2015), and titanite (e.g., Gordon et al., 2021), which have temperature sensitivities between >1200 °C and 600 °C. Similarly, timing and conditions of metasomatism can be constrained through petrochronology if dates can be linked with fluid-related alteration (e.g., coupled dissolution-precipitation) or new growth (Condit et al., 2018; Varga et al., 2020).

Apatite U-Pb has a temperature sensitivity of ~450–550 °C (Watson et al., 1985; Cherniak et al., 1991; Smye et al., 2018), dynamically recrystallizes during deformation (e.g.,

Nakano et al., 2001; Saka et al., 2008; Ribeiro et al., 2020), and is susceptible to dissolution-precipitation (Harlov, 2015). Apatite trace and rare earth element (TREE) geochemistry is a sensitive recorder of petrogenic processes during (re)crystallization (Belousova et al., 2002; Bruand et al., 2017). Therefore, apatite may be a robust tool for directly dating and geochemically characterizing deformation and metasomatism. However, it is critical to link U-Pb and TREE data to specific microstructures in order to understand how thermal, fluid, and deformation processes affect element distributions. We applied microstructural, TREE, and U-Pb mapping of apatite from an exhumed shear zone to gain quantitative insights into the nature, timing, and evolution of grain-scale deformation mechanisms and metasomatism.

GEOLOGIC SETTING, SAMPLES, AND METHODOLOGY

The Saint Barthélémy Massif (SBM) is located in the North Pyrenean Zone (NPZ), France (Fig. 1). The NPZ represents an inverted Creta-

ceous rift margin (e.g., Lagabrielle et al., 2010; de Saint Blanquat et al., 2016). In the SBM, an exhumed high-strain, ~100-m-thick, top-to-the-S (ultra)mylonitic shear zone, the Main Mylonitic Band (MMB; Figs. 1A and 1C), separates granites, migmatites, and mica schists in the hanging wall from middle- to lower-crustal amphibolite-granulite mylonitic gneisses in the footwall (Figs. 1A and 1B; e.g., Passchier, 1982; de Saint Blanquat et al., 1990). The MMB is a Cretaceous-aged, S-dipping, low-angle detachment that was tilted to a presently N-dipping position by Cenozoic shortening (Passchier, 1982, 1984; de Saint-Blanquat et al., 1986; Odlum and Stockli, 2020).

Previous major-element thermobarometry studies indicated that granulite-facies metamorphism occurred at ~700 °C and 5 kbar, followed by development of an initial foliation at ~600 °C and 3 kbar (de Saint Blanquat et al., 1990), which occurred between 300 and 280 Ma based on zircon and monazite U-Pb geochronology (Fig. 1A; Lemirre, 2018). The MMB developed through progressive strain localization within the deforming footwall gneisses during the retrograde evolution at temperatures between 550 and 450 °C (Passchier, 1984; de Saint Blanquat et al., 1990). MMB biotite and muscovite Ar-Ar ages (110–100 Ma; Costa and Maluski, 1988), apatite U-Pb ages from mylonitic gneisses (120–100 Ma; Figs. 1D and 1E; Odlum and Stockli, 2020), and titanite, rutile, and monazite U-Pb geochronology within talc-chlorite mineralization in the hanging wall (122–97 Ma; Boutin et al., 2016) indicate that the latest ductile deformation and metasomatism in the SBM occurred during Early Cretaceous rifting.

We chose samples (first characterized by Odlum and Stockli, 2020; Figs. 1D and 1F) from the MMB and footwall gneiss (FWG; Fig. 1). The MMB sample, 16-SB-14, yielded bulk sample apatite U-Pb dates between 300 and 100 Ma
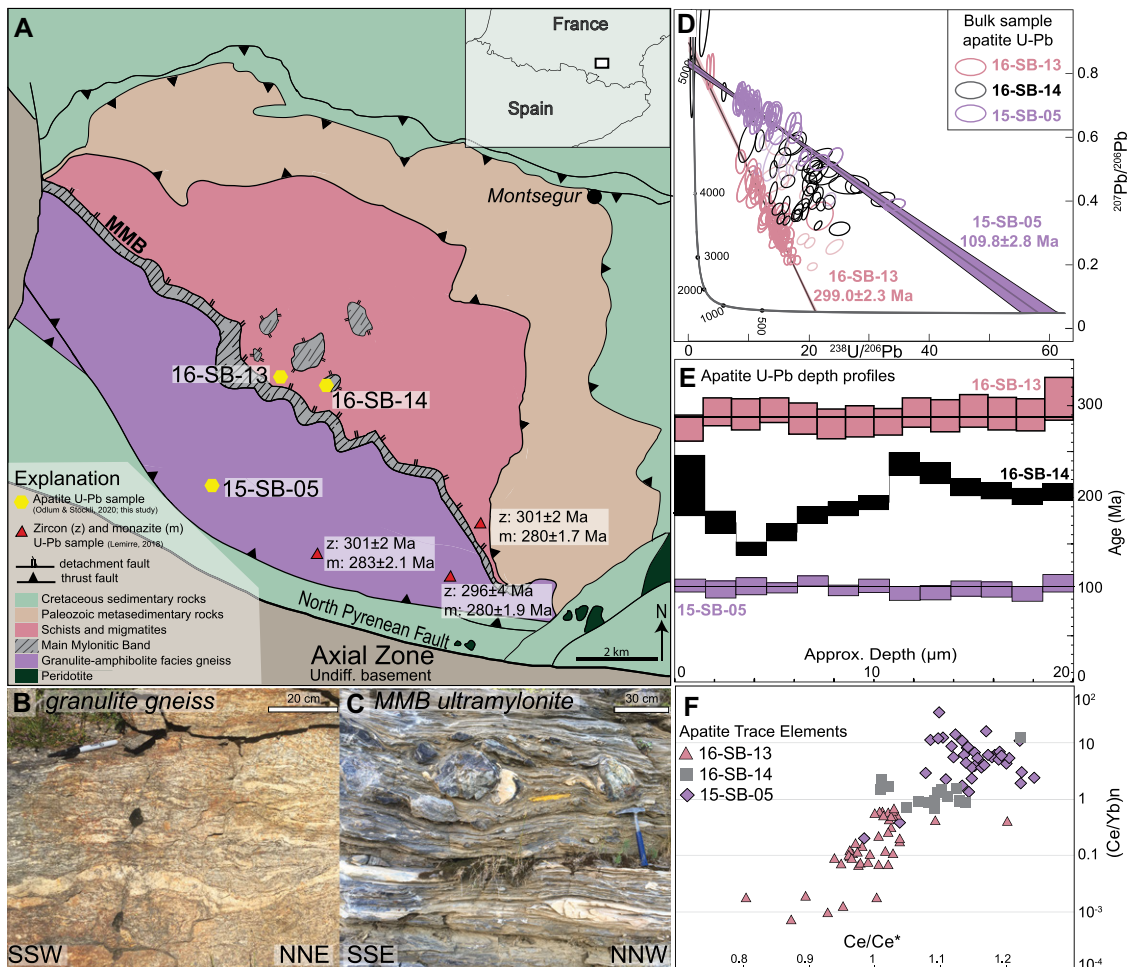
Figure 1. (A) Geologic map of Saint Barthelemy Massif, Pyrenees, France, with sample locations. (B–C) Field outcrop photographs of footwall gneisses (B) and Main Mylonitic Band (MMB) (C). (D) Bulk sample apatite U-Pb ages. (E) Representative single-grain U-Pb depth profiles. (F) Trace-element data (from Odlum and Stockli, 2020). Zircon and monazite U-Pb data are from Lemirre (2018).

(Figs. 1D and 1E). Sample 15-SB-05 was taken from a high-grade paragneiss with a bulk sample apatite U-Pb age of 109.8 ± 2.8 Ma, which was interpreted to record Early Cretaceous exhumation and(or) deformation, and enrichment in light rare earth elements (LREEs; Figs. 1D and 1F; Odlum and Stockli, 2020). The detailed methodology, including electron backscatter diffraction (EBSD) and laser ablation–inductively coupled plasma–mass spectrometry (LA-ICP-MS) operating conditions, is summarized in Supplemental Material[1].

APATITE MICROSTRUCTURES AND DEFORMATION MECHANISMS

FWG apatite exhibits internal lattice misorientation characteristic of crystal plasticity (Fig. 2; Figs. S1 and S2). EBSD maps display intragranular distortion expressed as lattice bending about the crystallographic $\langle a \rangle$ axis, concentrated at low-angle (<5°) dislocation boundaries (Figs. 2A and 2D). Misorientation profiles

---

[1]Supplemental Material. Detailed SEM and LA-ICP-MS methodologies, U-Pb and TREE data tables, and supplemental figures. Please visit https://doi.org/10.1130/GEOL.S.19233003 to access the supplemental material, and contact editing@geosociety.org with any questions.

(A-A′) exhibit 14° of cumulative misorientation in grain 334 (Fig. 2C) and 35° in grain 321 (Fig. 3E). Misorientation boundaries are consistently aligned parallel to the $\langle a \rangle$ axis and commonly transect the entire grain (Figs. 2A and 3E). Crystallographic axes are systematically dispersed around a common rotation axis (Fig. 2B), and the presence of discrete low-angle boundaries indicates a dislocation creep deformation mechanism (e.g., Reddy et al., 2006). Pole figures indicate that dislocation creep is accommodated by the $\{10\bar{1}0\}\langle 0001 \rangle$ (prism $\langle c \rangle$)) slip system (Figs. 2B and 2E), consistent with slip systems reported from apatite deformation experiments (Nakano et al., 2001; Saka et al., 2008). Low-angle misorientation inverse pole figures (IPF) for grains 334 and 321 (Figs. 2A and 3E) indicate basal $\langle a \rangle$ and prism $\langle c \rangle$ slip systems, and potentially rhomb $\langle a \rangle$ slip in grain 321.

EBSD data from MMB apatite provide evidence for dislocation creep, but most grains show limited to no lattice bending or low-angle boundaries (Figs. 2D and 4E; Figs. S1 and S3). Grain 202 displays intragranular misorientation concentrated along low-angle boundaries oriented parallel to the $\langle a \rangle$ axis (Fig. 2F) that accommodate ≤2° of misorientation, and cumulatively <6° of lattice bending across the

grain (Fig. 2D). Crystallographic orientations along a diffuse low-angle boundary exhibit a systematic dispersion consistent with prism $\langle c \rangle$ slip (Fig. 2E), and the IPF shows basal $\langle a \rangle$ and prism $\langle c \rangle$ slip. Other MMB grains display low to no lattice misorientation, with some weak intragranular misorientation patterns that lack well-defined low-angle boundaries, and yield random IPFs (Fig. 4E; Fig. S3).

TREE AND U-Pb RESULTS

FWG apatite TREE maps (Fig. 3C) display two patterns. Sr, Y, and La, Ce (LREEs) show patterns defined by significant variation in concentrations (tens to hundreds of parts per million) subparallel to the apatite $\langle c \rangle$ axis, and nearly orthogonal to low-angle boundaries (Fig. 3C). Eu exhibits a similar pattern with less variation (<10 ppm). Yb and Lu (heavy [H] REEs) are generally uniform, with concentrations varying between 1 and 10 ppm (Fig. 3C). TREE patterns in MMB grains are patchy and characterized by significant variations in concentration (tens to hundreds of parts per million; Fig. 4C) that, to first order, coincide with dark and bright zones in cathodoluminescence (CL) images (Figs. 4A and 4C). The lowest LREE and Eu concentration zones are collocated with dislocation arrays (Figs. 4B and 4C). Y and HREEs generally have
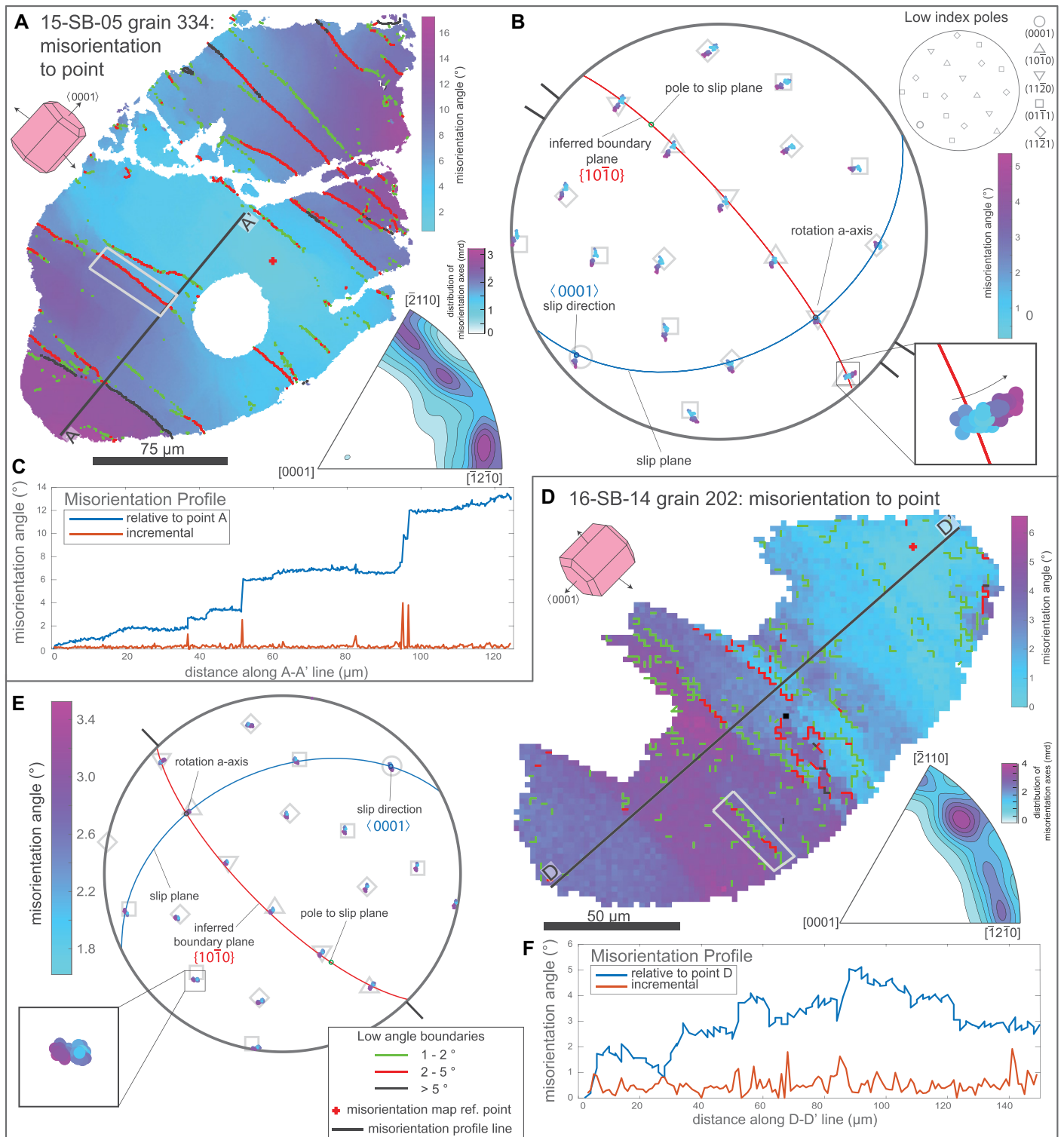
Figure 2. (A, D) Electron backscatter diffraction (EBSD) misorientation to point maps, (B, E) pole figures of subset area (gray boxes in A and D), with black ticks denoting strike of subset boundaries, and (C, F) misorientation profiles. Laser-ablation pits are from previous analysis of Odlum and Stockli (2020), summarized in Figure 1.

higher concentrations in the center that decrease toward the rim, with a secondary, more subtle variation that appears to mirror patchy CL patterns (Figs. 4A and 4C).

U-Pb dates in the FWG (15-SB-05 grain 321) are ca. 120–100 Ma, with a small area of ca. 300 Ma (Fig. 3F). The MMB apatite (16-SB-14

grain 220) U-Pb dates range between ca. 300 and 100 Ma (Fig. 4F) with a patchy pattern (Figs. 4D and 4F). Mapped dates and single-grain Tera-Wasserburg concordia plots (Figs. S1 and S2) yield consistent dates/date ranges as compared to bulk sample U-Pb dates (Figs. 1D and 1E; Odlum and Stockli, 2020).

DISCUSSION
Crystal Plastically Deformed Apatite

The U-Pb date pattern is evidence of heterogeneous radiogenic Pb (Pb*) loss across the grain at ca. 100 Ma. There is a small area of ca. 300 Ma (Fig. 3F), which is likely a relict portion of the grain preserving the original apatite age,
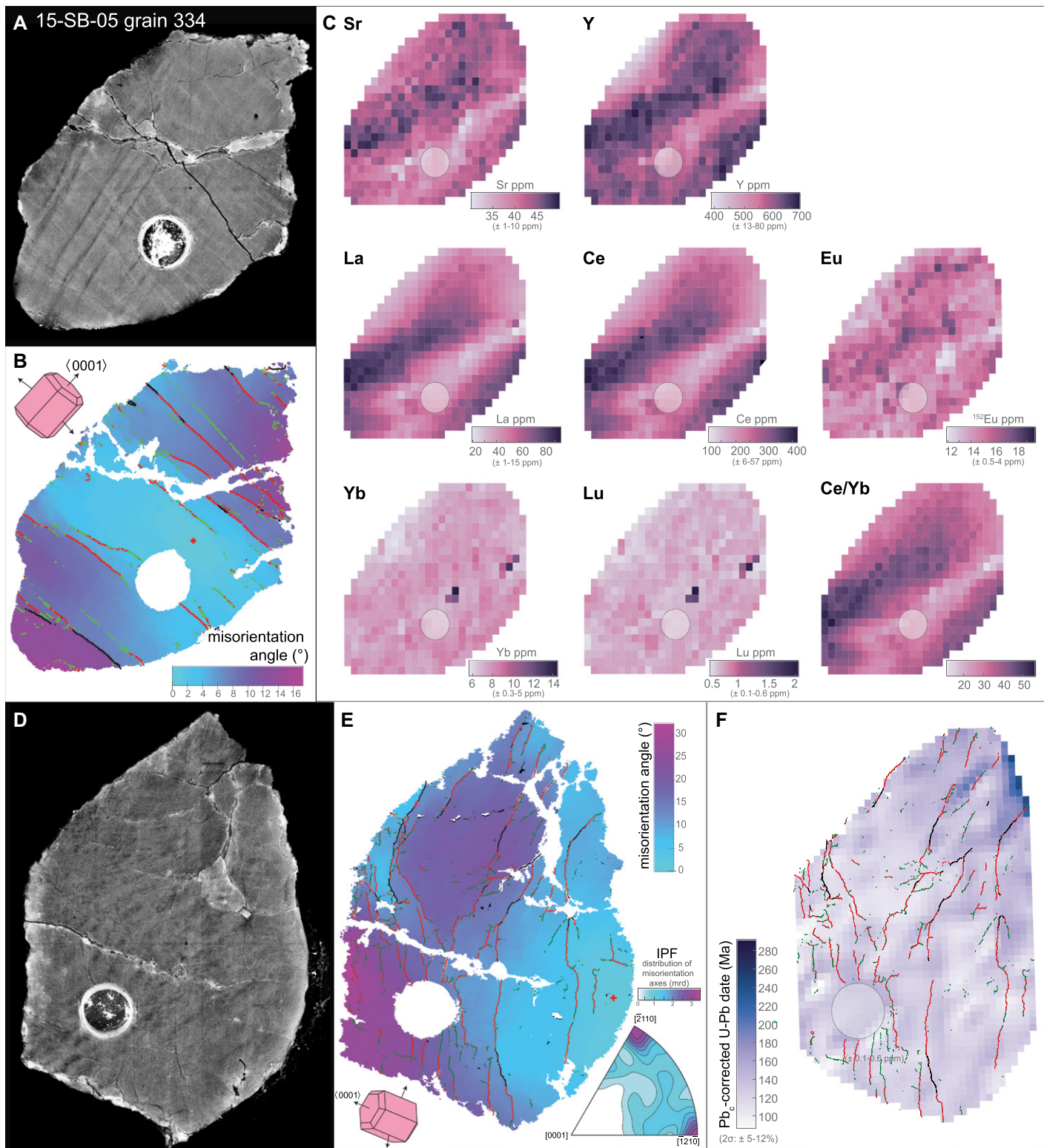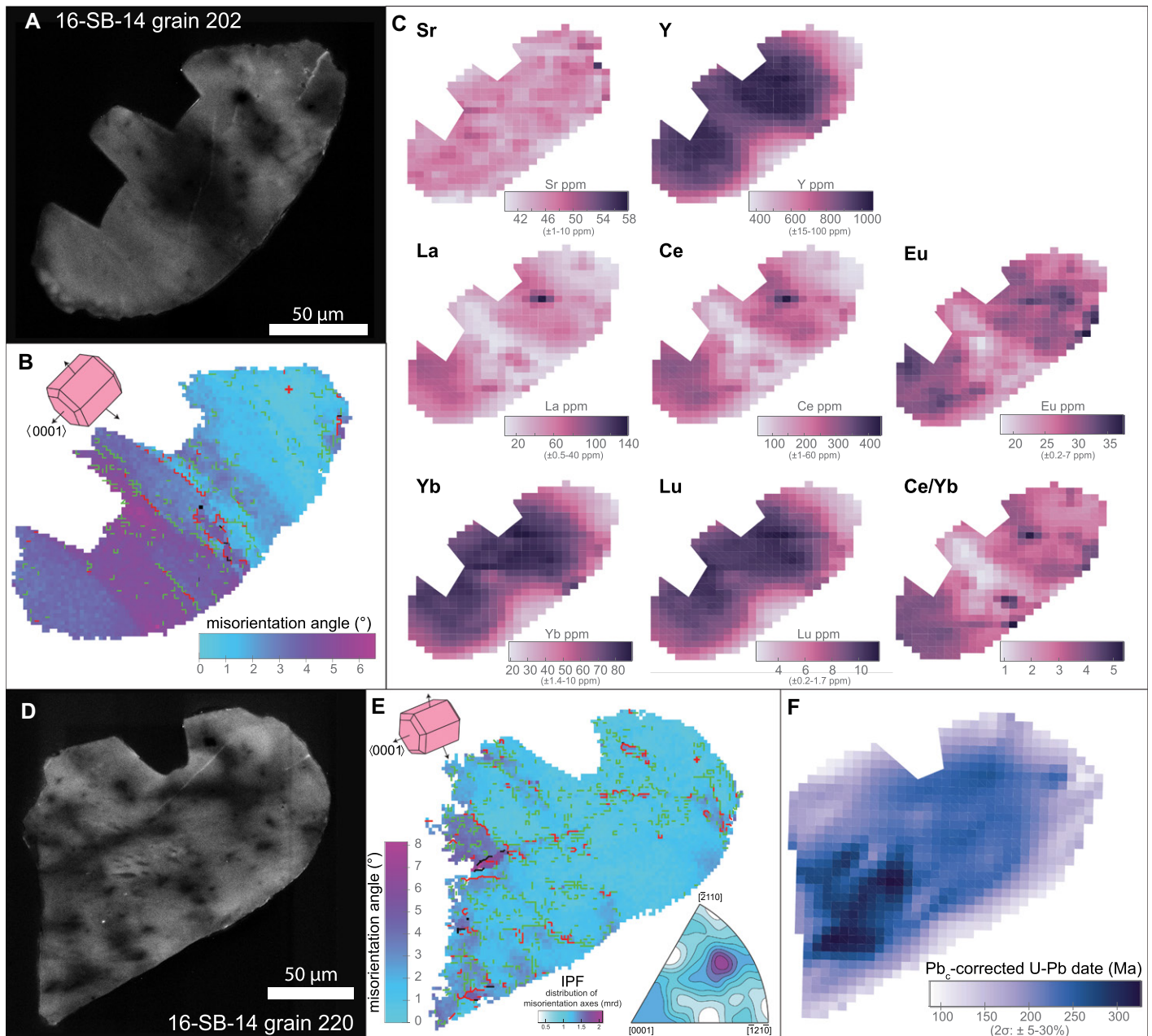
Figure 3. Footwall gneiss sample 15-SB-05 apatite. (A) Grain 334 cathodoluminescence (CL) image, (B) electron backscatter diffraction (EBSD) misorientation to point map, and (C) trace and rare earth element (TREE) maps. (D) Grain 321 CL image, (E) EBSD misorientation to point map, and (F) U-Pb date map. See the legend in Figure 2 for boundary lines in B and E. IPF—inverse pole figure.

which overlaps with zircon and monazite U-Pb ages in these units (Lemirre, 2018) and hanging-wall apatite ages (Fig. 1D), supporting the interpretation that ca. 120–100 Ma dates are isotopically reset ages (i.e., Pb* loss) and not Early Cretaceous neoblastic apatite. We did not ob-serve rim-to-core U-Pb date diffusional profiles that would indicate dates are simple thermochronologic cooling ages associated only with thermally activated Pb volume diffusion. Instead, the U-Pb age pattern coincides with low-angle boundaries to first order (Fig. 3F). Dislocation arrays may act as fast pathways for Pb* diffusion out of grains, similar to proposed mechanisms in monazite (Erickson et al., 2015) and zircon (Reddy et al., 2007; Moser et al., 2009; Timms et al., 2011; Piazolo et al., 2012, 2016). We suggest that progressive deformation led to

Figure 4. Main Mylonitic Band (MMB) sample 16-SB-14 apatite. (A) Grain 202 cathodoluminescence (CL) image, (B) electron backscatter diffraction (EBSD) misorientation to point map, and (C) trace and rare earth element (TREE) maps. (D) Grain 220 CL image, (E) EBSD misorientation to point map, and (F) U-Pb date map. See the legend in Figure 2 for boundary lines in B and E. IPF—inverse pole figure.

sweeping of Pb* to dislocation arrays followed by pipe diffusion out of the crystal (Piazolo et al., 2012, 2016), and thus U-Pb dates reflect and were also governed by intragrain misorientation boundaries. These observations together with mylonitization temperatures of 450–550 °C (de Saint Blanquat et al., 1990) indicate that deformation and Pb* loss processes were likely coeval, and thus deformed apatite U-Pb ages directly date ductile deformation.

The Sr, Y, Eu, and LREE patterns are distinct from microstructural patterns and U-Pb date patterns. We suggest that these elements preserve higher-temperature processes than U-Pb because TREEs are only mobile in apatite at higher

temperatures ($\geq$700–800 °C) than Pb ($\geq$450–550 °C; Cherniak, 2010). Possible scenarios for observed patterns are (1) TREE diffusion parallel to the $\langle c \rangle$ axis (fast diffusion pathways; Dykes, 1971; Iqdari et al., 2003) at temperatures $\geq$700–800 °C, (2) a different dominant slip system operative in apatite at higher temperatures (similar to quartz slip behaviors) that may control TREE patterns, or (3) a combination of the two. If apatite slip systems are temperature sensitive, then higher-temperature slip systems could have created dislocation arrays parallel to the $\langle c \rangle$ axis (via prism $\langle a \rangle$ or basal $\langle a \rangle$) that controlled TREE diffusion (e.g., Chapman et al., 2019). IPFs of deformed grains support the in-

ference that these slip systems were active at some point. Further work characterizing apatite deformation at various temperatures is necessary, but both scenarios suggest that TREEs capture higher-temperature processes (e.g., the 700 °C metamorphism event), and together with U-Pb ages and microstructures, they can provide a more complete record of the prograde and retrograde evolution of rock units.

Metasomatized Apatite

Patchy MMB apatite textures in CL images, U-Pb dates, and TREE maps (16-SB-14 grain 220) are collectively interpreted as evidence of coupled dissolution-precipitation reactions

(Fig. 4F). Patchy patterns may indicate enhanced fluid infiltration into grains due to (1) pervasive, interconnected, three-dimensional micro- and nanoporosity developed during dissolution-precipitation reactions (Harlov et al., 2005; Putnis, 2009), and(or) (2) cracks or subgrain/low-angle boundaries formed during crystal plastic deformation. The 300 Ma dates overlap with zircon U-Pb ages from these units (Lemirre, 2018), suggesting that these domains represent unreacted portions maintaining the original age. The youngest 120 to 100 Ma dates represent reacted, or reprecipitated, apatite (Fig. 4F). Dates falling between 300 and 100 Ma may represent some inheritance of less mobile elements (including U, Th, and Pb systematics) from precursor apatite (Varga et al., 2020), portions of the grain that have undergone partial resetting, and(or) domain mixing within the 12 μm laser spot size during analysis. Dates between 300 and 100 Ma, which also make up the wedge shape in Terra-Wasserburg space (Fig. 1D; Fig. S5), are likely geologically meaningless, with the true age of metasomatism represented by the youngest cluster of dates (Varga et al., 2020).

The TREE maps patterns mirror CL zoning (Figs. 4A and 4C), which we interpret to reflect domains of original and reprecipitated apatite. Bright areas in CL correspond to areas with higher LREE concentrations (Figs. 4A and 4C), which likely represent reacted portions of grains, based on prior work that suggested reprecipitated apatite is enriched in LREEs relative to HREE and hanging-wall apatite (Fig. 1F; Odlum and Stockli, 2020). The HREEs and Y display patterns distinct from LREEs and Eu. The difference in behavior between LREE and Eu versus HREE and Y may be explained by (1) HREE and Y are less incompatible elements and less fluid-mobile elements, so they are less affected by dissolution-precipitation processes, or (2) the fluids did not contain significant HREEs or Y, so reprecipitated apatite maintained concentrations similar to original apatite. While both factors were likely at play, we favor the interpretation that fluid composition was the dominant control, because prior work has shown that HREE-rich fluid composition can enrich apatite in HREEs (e.g., Glorie et al., 2019).

Most MMB apatite grains display low to no lattice misorientations (Figs. 4B and 4E; Fig. S3). Internal misorientations may have been a result of earlier crystal plastic deformation that was subsequently overprinted by dissolution-precipitation (i.e., partial replacement reactions with a high degree of epitaxy) or a direct effect of the dissolution-precipitation process itself (Spruzeniece et al., 2017). We favor the interpretation that most dislocation arrays were created as apatite was deforming via dislocation creep, and as rocks were exhumed and strain and fluids were progressively localized to form the MMB, dissolution-precipitation reactions variably overprinted microstructures.

Challenges and Opportunities in Apatite Petrochronology

Apatite petrochronology is a robust tool for constraining the timing and geochemistry of the most recent deformation and(or) fluid-rock interaction event. Crystal plastic deformation microstructures can change apatite chemical and age signatures. Apatite U-Pb dates can be reset in deformed apatite, with the youngest date representing the age of the last major deformation event. Similarly, in fluid-altered apatite, the youngest dates are robust for constraining the timing of the latest dissolution-precipitation and(or) chemical exchange. Older dates obtained may or may not represent the original apatite age, and a priori or complementary zircon U-Pb ages are necessary to interpret the older apatite dates.

LA-ICP-MS maps showed several important geochemical relationships. LREEs and HREEs behave differently in both deformed and metasomatized grains. LREEs and Eu show greater variation and appear more affected by deformation and metasomatism. Decoupling between TREEs and U-Pb behavior in the FWG (Fig. 3), which has also been observed in titanite (Gordon et al., 2021), suggests that TREEs record higher-temperature processes than respective U-Pb systems. Future work characterizing apatite deformation mechanisms and isotopic signatures at variable *P-T* conditions is necessary to fully understand these relationships. Fluid-mediated replacement reactions affect TREE and U-Pb systems, and in reprecipitated apatite, the U-Pb and TREE values record the age and geochemistry of metasomatism, respectively. Microstructural analysis and(or) single-grain depth profile analysis are(is) critical for robust apatite U-Pb date interpretation. Significant intragrain TREE concentration variations can occur, and CL images can aid in accurate geochemical characterization. The presented approach is powerful for in situ apatite petrochronologic studies and a robust tool in ductile shear zones, metasomatized rocks including those at ambient temperatures <450 °C (e.g., fluid-rock interactions in brittle faults, mineral deposits of economic interest), and exhumed subduction zone complexes.

REFERENCES CITED
Belousova, E.A., Griffin, W.L., O'Reilly, S.Y., and Fisher, N.I., 2002, Apatite as an indicator mineral for mineral exploration: Trace-element compositions and their relationship to host rock type: Journal of Geochemical Exploration, v. 76, p. 45–69, https://doi.org/10.1016/S0375-6742(02)00204-2.

Boutin, A., de Saint Blanquat, M., Poujol, M., Boulvais, P., de Parseval, P., Rouleau, C., and Robert, J.F., 2016, Succession of Permian and Mesozoic metasomatic events in the eastern Pyrenees with emphasis on the Trimouns talc-chlorite deposit: International Journal of Earth Sciences, v. 105, p. 747–770, https://doi.org/10.1007/s00531-015-1223-x.

Bruand, E., Fowler, M., Storey, C., and Darling, J., 2017, Apatite trace element and isotope applications to petrogenesis and provenance: The American Mineralogist, v. 102, p. 75–84, https://doi.org/10.2138/am-2017-5744.

Chapman, T., Clarke, G.L., Piazolo, S., Robbins, V.A., and Trimby, P.W., 2019, Grain-scale dependency of metamorphic reaction on crystal plastic strain: Journal of Metamorphic Geology, v. 37, p. 1021–1036, https://doi.org/10.1111/jmg.12473.

Cherniak, D.J., 2010, Diffusion in accessory minerals: Zircon, titanite, apatite, monazite and xenotime: Reviews in Mineralogy and Geochemistry, v. 72, p.827–869, https://doi.org/10.2138/rmg.2010.72.18.

Cherniak, D.J., Lanford, W.A., and Ryerson, F.J., 1991, Lead diffusion in apatite and zircon using ion implantation and Rutherford backscattering techniques: Geochimica et Cosmochimica Acta, v. 55, p. 1663–1673, https://doi.org/10.1016/0016-7037(91)90137-T.

Condit, C.B., Mahan, K.H., Curtis, K.C., and Möller, A., 2018, Dating metasomatism: Monazite and zircon growth during amphibolite facies albitization: Minerals (Basel), v. 8, p. 187, https://doi.org/10.3390/min8050187.

Costa, S., and Maluski, H., 1988, Use of the ^{40}Ar-^{39}Ar stepwise heating method for dating mylonite zones: An example from the St. Barthélémy Massif (northern Pyrenees, France): Chemical Geology–Isotope Geoscience Section, v. 72, p. 127–144, https://doi.org/10.1016/0168-9622(88)90061-9.

de Saint-Blanquat, M., Brunel, M., and Mattauer, M., 1986, Les zones de cisaillement du massif Nord-pyrénéen du Saint-Berthélémy témoins probables de l'extension crustale d'âge crétacé: Comptes rendus de l'Académie des sciences: Série 2, Mécanique, Physique, Chimie, Sciences de l'univers, Sciences de la Terre, v. 303, p.1339–1344.

de Saint Blanquat, M., Lardeaux, J.M., and Brunel, M., 1990, Petrological arguments for high-temperature extensional deformation in the Pyrenean Variscan crust (Saint Barthélémy Massif, Ariège, France): Tectonophysics, v. 177, p. 245–262, https://doi.org/10.1016/0040-1951(90)90284-F.

de Saint Blanquat, M., Bajolet, F., Grand'Homme, A., Proietti, A., Zanti, M., Boutin, A., Clerc, C., Lagabrielle, Y., and Labaume, P., 2016, Cretaceous mantle exhumation in the central Pyrenees: New constraints from the peridotites in eastern Ariège (North Pyrenean zone, France): Comptes Rendus Geoscience, v. 348, p. 268–278, https://doi.org/10.1016/j.crte.2015.12.003.

Dykes, E., 1971, Diffusion anisotropy in apatite: Nature, Physical Science [London], v. 233, p. 12–13, https://doi.org/10.1038/physci233012b0.

Erickson, T.M., Pearce, M.A., Taylor, R.J.M., Timms, N.E., Clark, C., Reddy, S.M., and Buick, I.S., 2015, Deformed monazite yields high-temperature tectonic ages: Geology, v. 43, p. 383–386, https://doi.org/10.1130/G36533.1.

Glorie, S., Jepson, G., Konopelko, D., Mirkamalov, R., Meeuws, F., Gilbert, S., Gillespie, J., Collins,

A.S., Xiao, W., Dewaele, S., and De Grave, J., 2019, Thermochronological and geochemical footprints of post-orogenic fluid alteration recorded in apatite: Implications for mineralisation in the Uzbek Tian Shan: Gondwana Research, v. 71, p. 1–15, https://doi.org/10.1016/j.gr.2019.01.011.

Gordon, S.M., Kirkland, C.L., Reddy, S.M., Blatchford, H.J., Whitney, D.L., Teyssier, C., Evans, N.J., and McDonald, B.J., 2021, Deformation-enhanced recrystallization of titanite drives decoupling between U-Pb and trace elements: Earth and Planetary Science Letters, v. 560, 116810, https://doi.org/10.1016/j.epsl.2021.116810.

Harlov, D.E., 2015, Apatite: A fingerprint for metasomatic processes: Elements, v. 11, p. 171–176, https://doi.org/10.2113/gselements.11.3.171.

Harlov, D.E., Wirth, R., and Förster, H.J., 2005, An experimental study of dissolution-reprecipitation in fluorapatite: Fluid infiltration and the formation of monazite: Contributions to Mineralogy and Petrology, v. 150, p. 268–286, https://doi.org/10.1007/s00410-005-0017-8.

Iqdari, A., Velde, B., Benalioulhaj, N., Dujon, S.C., and El Yamine, N., 2003, Exchange of light rare earths for Ca in apatite: Comptes Rendus Geoscience, v. 335, p. 381–390, https://doi.org/10.1016/S1631-0713(03)00053-1.

Lagabrielle, Y., Labaume, P., and de Saint Blanquat, M., 2010, Mantle exhumation, crustal denudation, and gravity tectonics during Cretaceous rifting in the Pyrenean realm (SW Europe): Insights from the geological setting of the lherzolite bodies: Tectonics, v. 29, TC4012, https://doi.org/10.1029/2009TC002588.

Lemirre, B., 2018, Origin and Development of Thermicity in the Varis Pyrenees (Ph.D. dissertation): Toulouse, France, Université Paul Sabatier-Toulouse III, 290 p.

Moser, D.E., Davis, W.J., Reddy, S.M., Flemming, R.L., and Hart, R.J., 2009, Zircon U-Pb strain chronometry reveals deep impact-triggered flow: Earth and Planetary Science Letters, v. 277, p. 73–79, https://doi.org/10.1016/j.epsl.2008.09.036.

Nakano, T., Awazu, T., and Umakoshi, Y., 2001, Plastic deformation and operative slip system in mineral fluorapatite single crystal: Scripta Materialia,

v. 44, p. 811–815, https://doi.org/10.1016/S1359-6462(00)00656-4.

Odlum, M.L., and Stockli, D.F., 2020, Geochronologic constraints on deformation and metasomatism along an exhumed mylonitic shear zone using apatite U-Pb, geochemistry, and microtextural analysis: Earth and Planetary Science Letters, v. 538, 116177, https://doi.org/10.1016/j.epsl.2020.116177.

Passchier, C.W., 1982, Pseudotachylyte and the development of ultramylonite bands in the Saint-Barthelemy Massif, French Pyrenees: Journal of Structural Geology, v. 4, p. 69–79, https://doi.org/10.1016/0191-8141(82)90008-6.

Passchier, C.W., 1984, Fluid inclusions associated with the generation of pseudotachylyte and ultramylonite in the French Pyrenees: Bulletin de Minéralogie, v. 107, p. 307–315.

Piazolo, S., Austrheim, H., and Whitehouse, M., 2012, Brittle-ductile microfabrics in naturally deformed zircon: Deformation mechanisms and consequences for U-Pb dating: The American Mineralogist, v. 97, p. 1544–1563, https://doi.org/10.2138/am.2012.3966.

Piazolo, S., La Fontaine, A., Trimby, P., Harley, S., Yang, L., Armstrong, R., and Cairney, J.M., 2016, Deformation-induced trace element redistribution in zircon revealed using atom probe tomography: Nature Communications, v. 7, p. 1–7, https://doi.org/10.1038/ncomms10490.

Putnis, A., 2009, Mineral replacement reactions: Reviews in Mineralogy and Geochemistry, v. 70, p. 87–124, https://doi.org/10.2138/rmg.2009.70.3.

Reddy, S.M., and Potts, G.J., 1999, Constraining absolute deformation ages: The relationship between deformation mechanisms and isotope systematics: Journal of structural Geology, v. 21, p.1255–1265, https://doi.org/10.1016/S0191-8141(99)00032-2.

Reddy, S.M., Timms, N.E., Trimby, P., Kinny, P.D., Buchan, C., and Blake, K., 2006, Crystal-plastic deformation of zircon: A defect in the assumption of chemical robustness: Geology, v. 34, p. 257–260, https://doi.org/10.1130/G22110.1.

Reddy, S.M., Timms, N.E., Pantleon, W., and Trimby, P., 2007, Quantitative characterization of plastic

deformation of zircon and geological implications: Contributions to Mineralogy and Petrology, v. 153, p. 625–645, https://doi.org/10.1007/s00410-006-0174-4.

Ribeiro, B.V., Lagoeiro, L., Faleiros, F.M., Hunter, N.J.R., Queiroga, G., Raveggi, M., Cawood, P.A., Finch, M., and Campanha, G.A.C., 2020, Strain localization and fluid-assisted deformation in apatite and its influence on trace elements and U-Pb systematics: Earth and Planetary Science Letters, v. 545, 116421, https://doi.org/10.1016/j.epsl.2020.116421.

Saka, H., Goto, D. and Moon, W.J., 2008, Dislocations in plastically deformed apatite: Journal of Materials Science, v. 43, p. 3234–3239, https://doi.org/10.1007/s10853-008-2551-z.

Smye, A.J., Marsh, J.H., Vermeesch, P., Garber, J.M., and Stockli, D.F., 2018, Applications and limitations of U-Pb thermochronology to middle and lower crustal thermal histories: Chemical Geology, v. 494, p. 1–18, https://doi.org/10.1016/j.chemgeo.2018.07.003.

Spruzeniece, L., Piazolo, S., and Maynard-Casely, H.E., 2017, Deformation-resembling microstructure created by fluid-mediated dissolution-precipitation reactions: Nature Communications, v. 8, p. 1–9, https://doi.org/10.1038/ncomms14032.

Timms, N.E., Kinny, P.D., Reddy, S.M., Evans, K., Clark, C., and Healy, D., 2011, Relationship among titanium, rare earth elements, U-Pb ages and deformation microstructures in zircon: Implications for Ti-in-zircon thermometry: Chemical Geology, v. 280, p. 33–46, https://doi.org/10.1016/j.chemgeo.2010.10.005.

Varga, J., Raimondo, T., Daczko, N.R., and Adam, J., 2020, Experimental alteration of monazite in granitic melt: Variable U-Th-Pb and REE mobility during melt-mediated coupled dissolution-precipitation: Chemical Geology, v. 544, 119602, https://doi.org/10.1016/j.chemgeo.2020.119602.

Watson, E.B., Harrison, T.M., and Ryerson, F.J., 1985, Diffusion of Sm, Sr, and Pb in fluorapatite: Geochimica et Cosmochimica Acta, v. 49, p. 1813–1823, https://doi.org/10.1016/0016-7037(85)90151-6.